LAF | https://doi.org/10.15302/J-LAF-2026-0025
Volume 14 / Issue 3 / 260025 / 2026
Received Date | 2025-10-15 Accepted Date | 2026-03-06
© Higher Education Press 2026

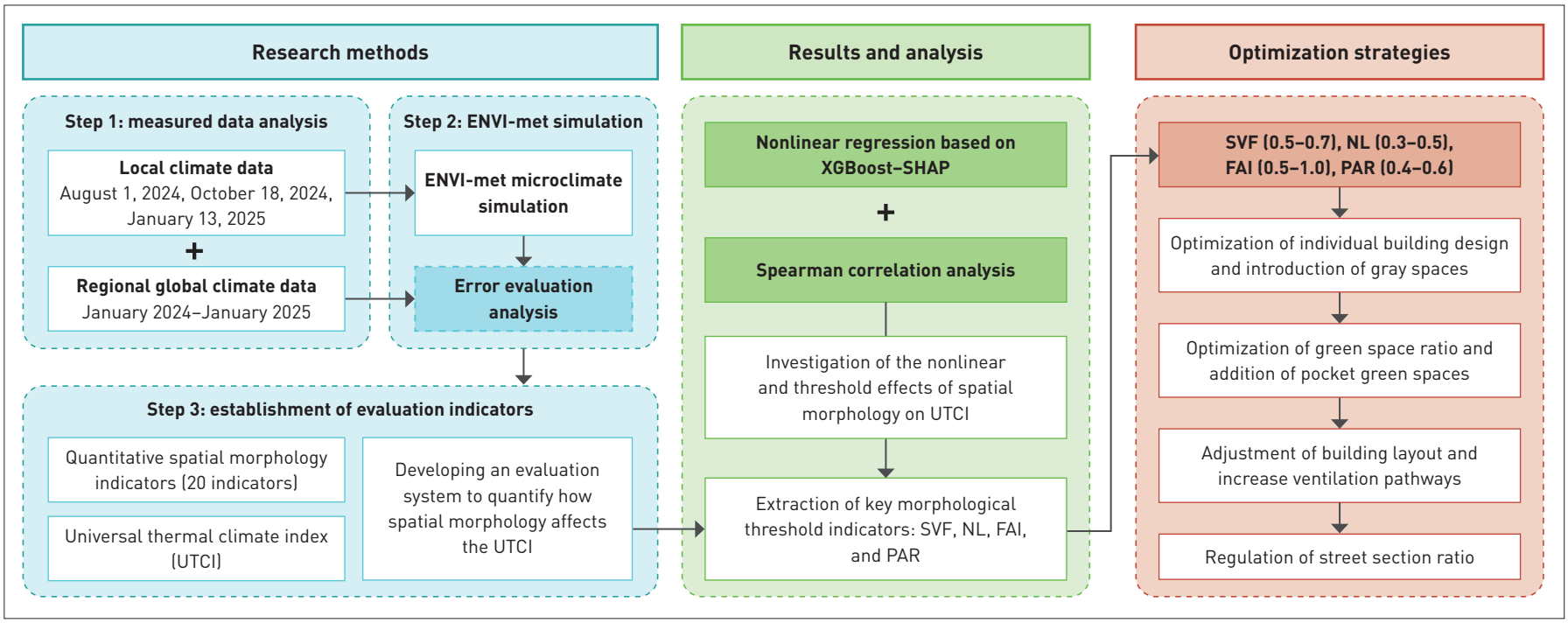
Thermal Environment Response Mechanism of Old Urban Blocks in Coastal County Towns of Southeast Zhejiang Based on a Multi-Season Empirical Analysis

Zhixing LI[1,2,*], Xiaoju LI[1], Mimi TIAN[1]

1 School of Design and Architecture, Zhejiang University of Technology, Hangzhou 310000, China
2 School of Built Environment and Construction, Politecnico di Milano, Milan 20133, Italy

*CORRESPONDING AUTHOR
Address: Pingfeng Campus, Zhejiang University of Technology, No. 288 Liuhe Road, Xihu District, Hangzhou 310000, China
Email: zxlee910@zjut.edu.cn

GRAPHICAL ABSTRACT



ABSTRACT

This study focuses on a typical old urban block in Rui'an City, Zhejiang Province, exploring the quantitative relationship between urban external morphology and human thermal comfort. The aim is to establish an evaluation index system for urban regeneration that is applicable to old urban blocks in coastal county towns. The study conducted a year-long meteorological observation and microclimate simulations to create a long-term dynamic monitoring sequence for the summer, transition, and winter seasons. It extracted 20 spatial morphology indicators and established an XGBoost-SHAP nonlinear regression model combined with the UTCI. The results indicate that: 1) air temperature, humidity, and wind speed exhibit significant variations across the three seasons due to differences in spatial morphology; 2) sky view factor (SVF), frontal area index (FAI), paved area ratio (PAR), and near-line ratio (NL) are key factors influencing courtyard thermal comfort; 3) the effects of different spatial morphology quantification indicators on thermal comfort vary significantly across different seasons. In winter, the optimal morphological ranges for thermal comfort are: SVF at 0.55–0.75,

NL at 0.03–0.10, FAI at 0.3–1.0, and PAR at 0.1–0.3, which strike a balance between shading, ventilation, thermal insulation, and the surface thermal environment. The study enriches theoretical research on the quantitative relationship between microclimates and spatial morphology, providing targeted optimization strategies in practice and offering data support and references for low-carbon urban regeneration and sustainable community development in coastal county towns of southeast Zhejiang.

KEYWORDS

Thermal Comfort; Urban Spatial Morphology; Microclimate Simulation; XGBoost–SHAP Model

HIGHLIGHTS

- Integrated field measurements, simulations, and morphology-based microclimate assessment
- Quantified seasonal thermal responses and comfort thresholds of SVF, NL, FAI, and PAR
- Translated microclimate mechanisms into regeneration-oriented urban design strategies

RESEARCH FUND

National Natural Science Foundation of China (No. 52308039)

1 Introduction

Urbanization is one of the most significant driving forces of global environmental change, and its progression exhibits pronounced disparities across countries and regions[1]. According to United Nations reports, the proportion of the global population residing in cities continues to increase, and high-density built environments have become spatial units where the impacts of climate change are most concentrated. Consequently, urban thermal environment regulation and climate adaptation have emerged as shared priorities in both international academic research and planning practice. Under the "carbon peaking and carbon neutrality" goals, national climate adaptation strategies, and the initiative of constructing climate-resilient cities, urban regeneration and the redevelopment of existing built-up areas are accelerating worldwide. In China, urbanization has entered a structural transition, shifting its focus from outward expansion to inward quality improvement[2–5]. Addressing heat risks and enhancing thermal safety and climate adaptability within existing high-density built environments have thus become fundamental scientific issues for sustainable urban development, making urban microclimate and human thermal comfort research essential for urban regeneration.

Rapid urbanization—marked by impervious surface expansion, increased building density, and reduced greenery—intensifies the urban heat island (UHI) effect and heat exposure, threatening public health, building energy efficiency, and urban resilience[6–7]. Consequently, thermal environment research has deepened across spatial scales. Macro-scale studies primarily focus on the relationships between land-use patterns, overall urban morphology, and regional heat island intensity[8–9]. Conversely, meso- and micro-scale research examines how morphological elements—such as street canyon aspect ratio (H/W), sky view factor (SVF), building compactness, ventilation potential, surface material properties, and vegetation structure—regulate local microclimates[10–11]. Recently, the research focus has shifted from simple temperature comparisons to process-based analyses involving radiation balance, turbulence characteristics, and wind field structures, elucidating the mechanisms underlying neighborhood-scale heat exposure.

Methodologically, the advanced microclimate simulation tools have enabled more refined analyses. Models (e.g., ENVI-met, RayMan, SOLWEIG, OpenFOAM) are widely applied to simulate radiation, wind environments, and thermal comfort, which have expanded from typical street canyons to high-density communities, historic districts, and urban regeneration areas[12–16]. Concurrently, spatial morphology quantification has evolved from traditional metrics (e.g., SVF, H/W, green coverage ratio) to a multidimensional system encompassing building form, underlying surface properties, tree canopy structure, ventilation corridor potential, and the spatial configuration of heat and cold sources. These developments provide a systematic parametric foundation for quantitatively examining morphology–microclimate relationships[17–20]. Furthermore, machine learning and multi-scenario simulations now enable the exploration of nonlinear mechanisms and the assessment of multi-scale coupling effects, yielding highly predictive analytical frameworks. Regarding outdoor thermal comfort[21–22], the universal thermal climate index (UTCI)—which comprehensively integrates air temperature, humidity, wind speed, and mean radiant temperature—has largely superseded traditional models, such as Predicted Mean Vote (PMV) and physiologically equivalent temperature (PET), due

to its superior applicability in urban open spaces, becoming the mainstream indicator in thermal comfort research[23–24].

In recent years, driven by rapid urbanization and spontaneous local development, neighborhoods with high-density, self-organized characteristics have become widespread in coastal county towns of southeast Zhejiang. Unlike planned developments, these high-density neighborhoods emerged organically around market demand and household-based activities, resulting in compact street networks, fragmented building interfaces, and uneven building volumes. They feature highly mixed land use, typically exhibiting compound patterns such as "shop-front and residential-rear" and "ground-floor commercial and upper-floor residential." Their development typically follows a trajectory of "residential establishment–embedding of household businesses–superimposition of production and commerce–spatial consolidation," making their microclimate regulation capacity highly sensitive to street scale, ventilation corridors, surface materials, and shading structures. Such old urban blocks are highly prevalent in cities including Wenzhou, Taizhou, as well as numerous county-level centers within southeast Zhejiang, serving as vital complements to government-led urban expansion.

Despite the rapid growth of related research, three prominent limitations remain. First, there is a clear "urban hierarchy bias" regarding research objects: existing studies largely focus on megacities (e.g., Beijing, Shanghai, Guangzhou), whereas the aforementioned self-organized neighborhoods have long been overlooked due to limited data availability and insufficient attention. Second, the temporal scope is often limited to single-season simulations, short time periods, or idealized meteorological conditions, failing to capture seasonal variability and the sensitivity and magnitude of morphological effects. Third, there is a lack of systematic quantitative indicator systems and integrated design guidelines tailored to specific neighborhood typologies, constraining practical implementation in urban regeneration.

To address these gaps, this study focuses on Cangqian Street in Rui'an City, Zhejiang Province, a representative old urban block in a coastal county town in southeast Zhejiang. Within a subtropical monsoon climate context, the study conducts long-term field measurements and ENVI-met simulations across seasons. A unified grid-based fishnet analysis method is proposed to construct a multidimensional spatial morphological indicator system. Air temperature, humidity, wind speed, solar radiation, and clothing thermal resistance are incorporated into a human thermal comfort calculation framework to achieve refined, multi-season comfort assessments. On this basis, key morphological indicators influencing the thermal environment and their mechanisms were identified, and microclimate-oriented design guidelines were proposed.

The contributions of this research are threefold. Theoretically, this study addresses the underrepresentation of urban hierarchy and spatial typologies in China's urban microclimate research, providing new empirical evidence. Methodologically, it establishes an integrated evaluation framework that couples long-term field measurements, multi-season simulations, and quantified morphological indicators, while introducing a unified fishnet analysis method to standardize spatial scales. Practically, it yields an actionable evaluation indicator system and targeted microclimate optimization strategies for high-density old urban blocks. The research outcomes offer robust data support and policy-relevant insights for sustainable, climate-resilient urban regeneration of old urban blocks in China.

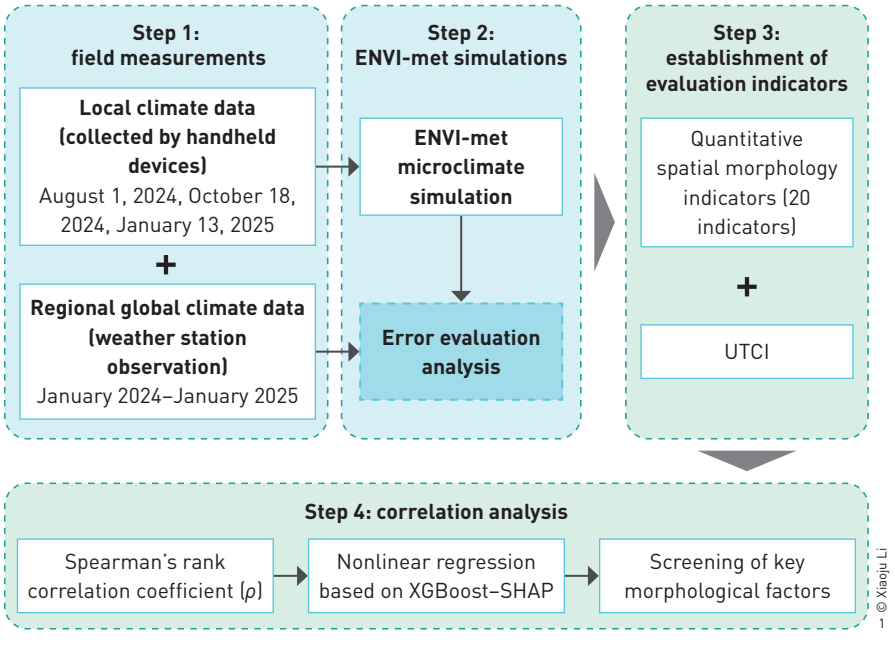
2 Research Methods

This study comprised four sequential steps: 1) field measurements, 2) ENVI-met simulations, 3) establishment of evaluation indicators, and 4) correlation analysis (Fig. 1).

2.1 Field Measurements

Given the pronounced variability of microclimatic conditions across spatial scales, a single data source cannot adequately characterize neighborhood thermal environments. Data were therefore collected at two levels (Table 1).

Fig. 1 Research methodology framework.



© Xiaoju Li

Table 1: Summary of measured parameters and utilized instruments

Category	Parameter	Instrument	Record collection interval	Precision	Measurement range
Regional measurements	Air temperature	Hobo U30-NRC Automatic Meteorological Station	1 h	±0.76 °C	±0.76 °C
	Relative humidity			±3%	±3%
	Rainfall			0.2 mm	0.2 mm
	Solar radiation			±10 W/m^2	±10 W/m^2
	Wind speed and direction			±0.5 m/s	±0.5 m/s
	Atmospheric pressure			±1.5 mbar	±1.5 mbar
Point measurements	Wind speed	AZ 8917 vane anemometer (10 cm vane)	1 h	±0.3 m/s	0–40 m/s
	Black ball temperature	AZ87786 wet bulb globe temperature data logger/ thermal index meter	1 h	±0.6 °C	–20–50 °C
	Air temperature			±0.6 °C	–20–50 °C
	Relative humidity			±3%	0–100%

1) Regional measurements. A HOBO U30-NRC automatic weather station was installed near the study area and operated continuously for one year (January 2024–January 2025). Unlike studies that rely on typical meteorological year data embedded in ENVI-met, this study used long-term *in situ* measurements as model inputs, improving the accuracy of boundary conditions and the reliability of simulations.

2) Point measurements. Field monitoring was conducted in representative street spaces. Parameters were measured using an AZ 8917 vane anemometer and an AZ87786 wet bulb globe temperature data logger/thermal index meter. All sensors were positioned at approximately 1.5 m above ground level, corresponding to pedestrian height and standard practice in microclimate and thermal comfort research. These data were used to quantify local microclimatic variations induced by different street morphologies and to determine the influence of spatial configuration on thermal conditions.

2.2 ENVI-met Simulations

2.2.1 Model Construction and Parameter Settings

ENVI-met is a three-dimensional microclimate simulation software based on computational fluid dynamics (CFD), which is widely used to evaluate the effects of buildings, vegetation, and surface environments on local climate and thermal comfort. It accounts for multiple influencing factors, including site conditions, building volumes, construction materials, and their physical properties. ENVI-met 5.2 (full version) was adopted in this study. A base model was constructed using unmanned aerial vehicle (UAV) imagery and 3D scanning data, with spatial modeling completed in AutoCAD and SketchUp. Geographic coordinates, spatial layers, and material properties were integrated using the INX plugin and Spaces module to generate the simulation file.

To balance accuracy and computational efficiency, the model resolution was configured as follows. The horizontal grid resolution (dX, dY) was set to 2 m to capture detailed geometric features of streets, courtyards, and building facades. Vertically, 35 grid layers were defined, corresponding to a maximum building height (H) of 15 m. The height of the first layer was set to 1.5 m to represent pedestrian level. Upper layers were increased with a stretching ratio of 15%. A buffer zone extending at least five times the maximum building height was added around the study area to minimize boundary effects.

2.2.2 Fishnet Analysis Method

The spatial texture of old urban blocks is highly irregular, limiting the effectiveness of conventional regularized methods. To address this, a fishnet analysis method was adopted. The study area was divided into 10 m × 10 m grid cells, and the simulated value at each cell center was used as the representative value for each unit. This approach enables the synchronized characterization of complex neighborhood morphology and microclimatic variables at a unified scale.

Subsequently, the simulated baseline climatic data were exported and post-processed in Excel, to generate a spatially explicit representation of thermal comfort across the study area. Through grid-based standardization, this method overcomes the scale inconsistency between morphological and environmental variables, improves the identification of microclimatic patterns in complex urban fabrics, and provides a more scientific and operational technical foundation for the regeneration and design of old urban blocks.

2.2.3 Error Evaluation Method

The purpose of error evaluation is to quantify the differences between simulated and measured data to ensure the validity of the simulation results. Commonly used metrics include the root mean square error (RMSE)[25] and the mean absolute percentage error (MAPE)[26]. RMSE reflects the overall magnitude of model error, while MAPE facilitates comparison across variables. The calculation formulas are as follows:

$$\mathrm{RMSE} = \sqrt{\frac{1}{n}\sum_{i=1}^{n}\left(y_i' - y_i\right)^2}, \tag{1}$$

$$\mathrm{MAPE} = \frac{1}{n}\sum_{i=1}^{n}\frac{|y_i' - y_i|}{y_i'} \times 100\%. \tag{2}$$

RMSE ranges from 0 to +∞, with lower values indicating higher accuracy. In this research, acceptable thresholds are 1.0 °C ≤ RMSE < 3.0 °C for air temperature and RMSE < 10% for relative humidity. MAPE also ranges from 0 to +∞ and is expressed as a percentage; values below 10% are considered acceptable.

2.3 Establishment of Evaluation Indicators

Microclimate impacts were evaluated by coupling the UTCI with urban spatial morphology. A systematic review was developed to quantify multi-scale morphological elements, including street layout, street canyon configuration, building clusters, and individual buildings. In combination with the landscape characteristics of old urban blocks, a quantified spatial morphological indicator system was established. Based on field measurements and ENVI-met–simulated meteorological data, UTCI values were extracted and compiled at the center of each grid. These values were matched with corresponding morphological indicators for comparative analysis to analyze how spatial configurations influence thermal comfort.

2.3.1 Quantified Spatial Morphological Indicators

A four-level indicator system comprising a total of 20 spatial morphology indicators[27–30] was established (Table 2). Spatial morphological indicators corresponding to each cell were extracted and assigned accordingly, enabling precise alignment between morphological metrics and microclimatic data. This approach facilitates the effective coupling of spatial form and microclimate conditions.

Table 2: Summary of spatial morphology indicators

Category	Indicator	Unit	Description	Calculation formula
Street layout	Distance-to-height ratio (DH)	—	The ratio of street distance to the average building height on both sides; larger values indicate a more open street canyon (less enclosure)	$\mathrm{DH} = \frac{D}{H}$
	Building height-to-street width ratio (HW)	—	The ratio of the average building height to the street width; larger values indicate a more enclosed, narrower street canyon (greater enclosure)	$\mathrm{HW} = \frac{H}{W}$
	SVF (source: Ref. [27])	—	The ratio of the observable sky area at a height of 1.5 m at a given location indicates the extent to which the area receives solar radiation or the degree of visual obstruction on the site	$\mathrm{SVF} = 1 - \sum_{i=1}^{n}\frac{\sin\gamma_i}{n}(n = 360)$

(Continued)

Table 2: Summary of spatial morphology indicators (Continued)

Category	Indicator	Unit	Description	Calculation formula
Street layout	Alley direction (Street θ)	(°)	The orientation angle of the alley's longitudinal axis relative to true north, from 0° to 180° (0° = true north, 180° = true south)	—
	Frontal area index (FAI)	—	The ratio of the windward area of a building in a specific direction to the total ground area	$\mathrm{FAI} = \frac{A_{\mathrm{proj}}}{A_{\mathrm{ground}}}$
	Unit parcel area standard deviation (A_SD)	—	The degree of dispersion of the area distribution of urban plots	$\mathrm{A_SD} = \sqrt{\frac{1}{n}\sum_{i=1}^{n}(A_i - \bar{A})^2}$
	Road network density (RD)	m^{-1}	The ratio of the total length of roads in a certain area to the area of that region	$\mathrm{RD} = \frac{L_{\mathrm{roads}}}{A_{\mathrm{area}}}$
	Near-line rate (NL) (source: Ref. [28])	—	A quantitative indicator used to measure the degree to which the street interface is close to or far from the street boundary, mainly used to describe the degree of variation in relief of the street interface	$\mathrm{NL} = \frac{L_{\mathrm{foreground}}}{L_{\mathrm{street}}} \times 100\%$
Building form	Building spacing (BL)	m	The horizontal distance between the outer walls of two buildings	$\mathrm{BL} = \frac{H}{\tan\theta}$
	Sunlight spacing factor (K)	—	In order to meet the sunlight requirements, the minimum distance between the front and rear buildings is proportional to the height of the front building	$\mathrm{K} = (H - H_1) \times \frac{1}{\tan h}$
Spatial configuration (source: Ref. [29])	Local choice (LC)	—	An indicator that measures the likelihood of a spatial unit being selected as a path within a local range	$\mathrm{LC} = \sum_{i=1}^{n} \frac{1}{d_i}$
	Local integration (LI)	—	An indicator measuring the degree of connectivity of a spatial unit with other spatial units within a local range	$\mathrm{LI} = \frac{n \times \left(\log_2\left(\frac{n+2}{3} - 1\right) + 1\right)}{(n-1)(\mathrm{MD}-1)}$
	Harmonic mean depth (HMD)	—	An indicator that measures the average distance of a spatial unit to all other spatial units	$\mathrm{HMD} = \frac{n}{\sum_{j=1}^{n} \frac{1}{d_{ij}}}$
	Relative entropy (RE)	—	An indicator that measures the difference between the connection distribution of a spatial unit and the connection distribution of the entire spatial unit	$\mathrm{RE} = \sum_{i=1}^{n} P_i \log\left(\frac{P_i}{q_i}\right)$
	Visual integration (VI)	—	An indicator that measures the degree of connectivity between the visual range of a spatial unit and the visual range of other spatial units	$\mathrm{VI} = \frac{1}{n}\sum_{i=1}^{n} V_i$
Landscape pattern	Number of patches (NP)	—	The total number of patches within a spatial unit	$\mathrm{NP} = \mathrm{count(patches)}$
	Landscape unit area rate (LA)	%	The proportion of a given landscape type area to the total spatial unit area	$\mathrm{LA} = \frac{A_{\mathrm{class}}}{A_{\mathrm{total}}} \times 100\%$
	Perimeter-area fractal dimension (PAFRAC)	—	An indicator used to describe the complexity of patch shapes in the landscape	$\mathrm{PAFRAC} = \frac{2 \times \log(P)}{\log(A)}$
	Green space rate (GR) (source: Ref. [30])	%	The ratio of the total area of various green spaces to the total land area within a certain land use range	$\mathrm{GR} = \frac{A_{\mathrm{green}}}{A_{\mathrm{total}}} \times 100\%$
	Paved area rate (PAR)	%	The ratio of the area of hard paving to the total land area within a certain area	$\mathrm{PAR} = \frac{S_1 + S_2 + S_3}{L_1 \times L_2} \times 100\%$

2.3.2 Human Thermal Comfort Assessment Method

Thermal comfort is a key determinant of urban environmental quality and design[31]. In this study, it refers to residents' perceived satisfaction with urban outdoor thermal conditions. Common indices include UTCI, PET, heat index, wind chill index, the wet bulb globe temperature, and air quality index. At the microclimate scale, UTCI provides a comprehensive representation of human physiological responses to combined thermal factors. It captures temporal variability and is applicable across climates, seasons, and spatial scales[32–34]. Accordingly, UTCI was selected as the thermal comfort evaluation metric in this study to characterize human comfort in outdoor environments.

ENVI-met 5.2 (full version) was employed for simulation①. The model outputs mean radiant temperature (T_{mrt}), air temperature (T_a), relative humidity (RH), and wind speed (V_e) for each grid cell using the Active Simulation module. These variables were subsequently inputs in the Python "pythermalcomfort" library, which implements the standard UTCI algorithm to batch-calculate UTCI values for each cell and time step.

2.4 Correlation Analysis

Prior to nonlinear modeling, Spearman's rank correlation coefficient (ρ) was applied to test the monotonic relationships between the 20 spatial morphological indicators and UTCI[35]. Statistical significance was evaluated using a two-tailed test ($p < 0.05$). Considering that diverse relationships may exist between urban canyon morphology and outdoor thermal comfort, all spatial morphology indicators were retained for subsequent analysis to explore their combined influence mechanisms.

Subsequently, an XGBoost-SHAP–based nonlinear regression model was employed to investigate the complex relationships. To address the inherent limited interpretability of gradient boosting ensembles, SHAP was introduced to quantify each indicators' marginal contribution to the model predictions, thereby revealing the nonlinear influence mechanisms of different morphological features on thermal comfort[36–37]. Modeling was implemented using the Python "xgboost" library (version 1.7.0). A combination of grid search and five-fold cross-validation was applied for systematic hyperparameter optimization, using RMSE as the evaluation metric. To prevent overfitting, the final selected parameter set was configured as follows: maximum tree depth = 6, learning rate = 0.1, subsample ratio = 0.8, feature sampling ratio = 0.8, and an early stopping round of 50.

① This study focuses on summer and winter as the two most environmentally stressful seasons. Spring and autumn, as transitional periods, exert less thermal stress and offer limited additional insight into the extreme performance of morphological regulation; therefore, they were not included in the simulation.

3 Case Study

3.1 Regional Characteristics

Rui'an, a typical coastal county-level city in southern Zhejiang Province, has experienced long-term urban development driven predominantly by the private-sector economy. This trajectory has formed a spatial pattern centered on small and medium-sized enterprises, household workshops, and street-front businesses, reflecting the characteristics of the "Wenzhou Model." Field investigations revealed that the Cangqian Street neighborhood exhibits an interwoven pattern of old and new buildings. It retains traditional commercial architectural forms, such as arcaded buildings (a recessed main entrance forming a semi-enclosed space) and recessed shop entrances (a mixed-use building with a ground-floor setback creating a covered walkway), alongside residential and commercial extensions constructed during various historical periods. Street-front interfaces are dominated by small-scale retails, whereas interior lanes are primarily residential, forming semi-enclosed courtyards and traditional alley-based living spaces known locally as "tan" (坦). The main street, approximately 5–6 m wide, accommodates primarily pedestrian and non-motorized traffic. The facade morphology is complex, exhibiting a high degree of functional mix. Public spaces consist mainly of fragmented street corners, small commercial setbacks, and pocket-sized open areas. Vegetation is sparsely distributed in a patch-like manner, reflecting a gradual "infill greening" approach under constrained land conditions.

Consequently, this compact old urban block—characterized by high density, mixed land use, and fine-grained spatial scales—exhibits a microclimate highly sensitive to ventilation organization and surface materials. It thus serves as a highly representative empirical setting for investigating thermal comfort mechanisms and climate-adaptive optimization in the context of stock-based urban regeneration.

3.2 Field Measurement Content and Scheme

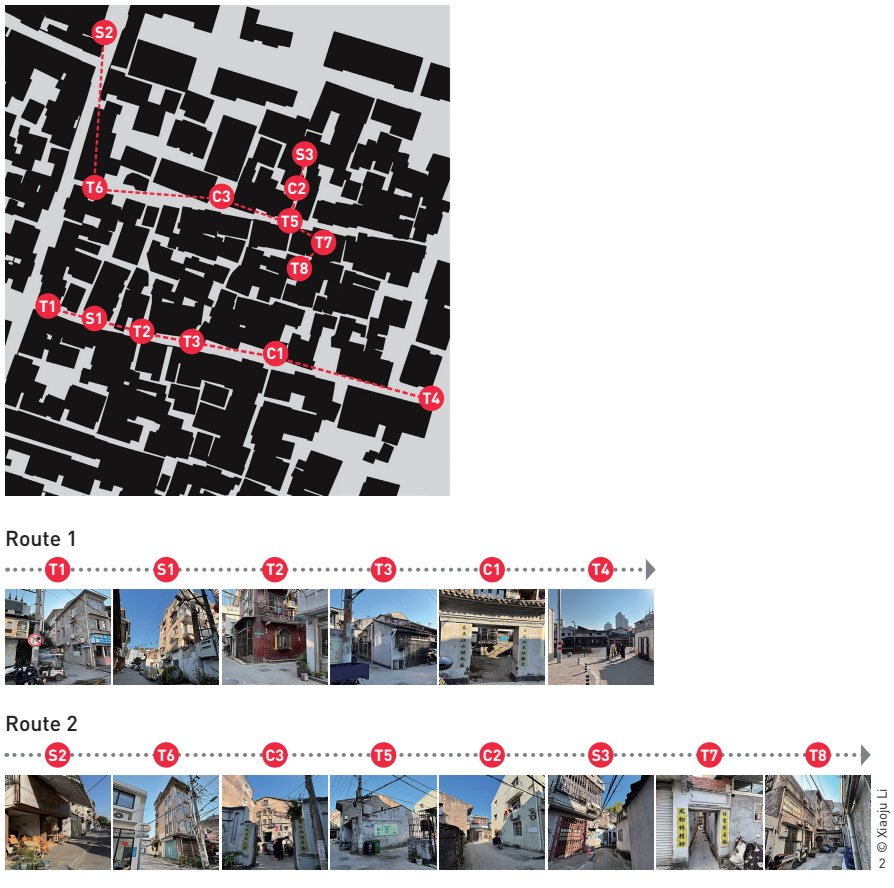
To ensure data representativeness and accuracy, an automatic weather station was installed on the unobstructed rooftop of the Yuhai No. 2 Primary School teaching building, approximately 20 m from Cangqian Street, minimizing anthropogenic disturbances. Continuous global observations were conducted from January 2024 to January 2025.

To explore the generalizable mechanisms linking spatial morphology and microclimate, seasonally representative baseline meteorological days were selected based on the 2023 Rui'an meteorological dataset. The selection procedure involved: 1) calculating monthly mean air temperature and relative humidity to establish seasonal baselines; 2) excluding days outside the 5th and 95th percentiles to eliminate extreme weather anomalies; and 3) selecting the typical meteorological day with a daily mean value closest to the monthly average with stable meteorological curves. Accordingly, August 1, 2024, October 18, 2024, and January 13, 2025 were chosen to represent summer, the transitional season, and winter, respectively. All selected days featured clear skies (cloud cover < 20%), moderate winds, and no precipitation, effectively representing baseline seasonal microclimates.

Measurement points were determined through stratified sampling based on UAV scanning and on-site surveys (Fig. 2). The neighborhood spatial system was deconstructed into three dominant space categories: alleys (T), courtyards (C), and transitional spaces (S). This classification corresponds to the three main spatial units commonly found in the neighborhood: circulation, commerce, and residence. Alleys function as connective circulation spaces; courtyards serve as residential microclimatic units; and transitional spaces (i.e., architectural "grey spaces" like arcades, shopfront canopies, and recessed entrance corridors) bridge indoor business activities and outdoor streets.

Based on morphological representativeness (covering variations in aspect ratio, orientation, and underlying surface conditions), functional relevance (nodes with intensive resident activities), and instrument accessibility, 14 measurement points were established: eight alley points (T1–T8), three courtyard points (C1–C3), and three transitional space points (S1–S3). This sample distribution proportionally reflects the actual spatial composition and usage characteristics of the site, ensuring effective representation. The field measurement scheme adopted a multi-point layout comprising two measurement routes, monitored synchronously by two investigators over a full day with a 1-hour sampling interval. These localized measurements were subsequently compared with corresponding weather station data for calibration and validation, thereby ensuring the scientific robustness and reliability of the dataset.

Fig. 2 Field measurement route map.



4 Results and Discussion

4.1 Field-Measured Characteristics of Neighborhood Microclimate

This section analyzes the results from two perspectives: comparing point-based measurements across seasons, and contrasting them with regional weather station data to explore the regulatory effects of spatial morphology on the microclimate. As shown in Figs. 3 and 4, nine representative points across three spatial types were selected for comparative analysis.

First, the point-based measurements exhibited significant seasonal variations (Fig. 3). Specifically, in summer, the temperature trends across all nine measurement points were broadly consistent. Air temperature increased gradually from 8:00 and reached its daytime peak between 14:00 and 15:00. Among the three spatial types, C spaces recorded the highest average temperatures (e.g., C1 reached 42.7 °C at 14:00), followed closely by T spaces (e.g., T2 reached 42.7 °C at 15:00). The lowest temperatures were observed in S spaces, with S1 dropping to 32.3 °C at 9:00. During the transitional season, C spaces exhibited the highest average temperatures. For example, C1 reached a maximum of 35.8 °C between 13:30 and 14:00. In winter, C spaces again showed the highest average temperatures. For example, C2 reached approximately 20 °C at 13:30 (actual maximum 20.1 °C at 13:32), while the highest among all points was 21.7 °C in C3 at 12:18.

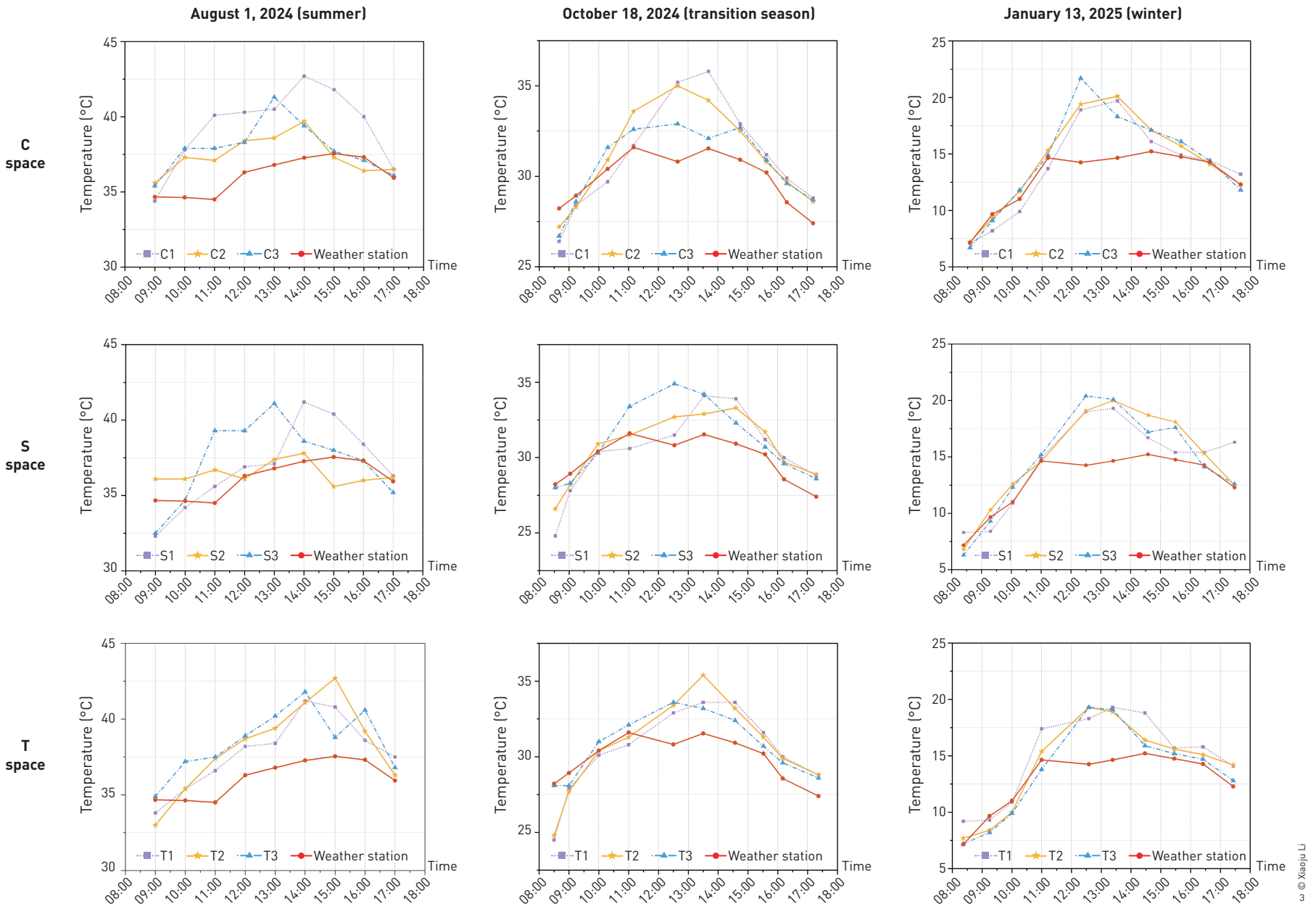


Fig. 3 Comparison of temperatures between regional and local climate data.

As shown in Fig. 4, relative humidity in the neighborhood exhibited an inverse diurnal pattern to air temperature across all three seasons, characterized by higher values in the morning and evening and lower values at midday. Specifically, in summer, the T spaces had the highest humidity levels. Among them, T3 recorded the highest relative humidity at approximately 74.1% at 9:00. In the transitional season, C spaces exhibited the highest relative humidity (approximately 58.9%), whereas T spaces showed the lowest (approximately 58.8%). At 13:30, S2 recorded the highest relative humidity at 50.6%. In winter, C spaces again showed the highest average relative humidity (34.8%), followed by T spaces (33.5%), while S spaces had the lowest average value (33.3%). At 13:30, the highest relative humidity was observed at T2 (25.8%).

Further comparison between local point measurements and regional weather station data revealed a consistent pattern of higher temperatures within the neighborhood. Specifically, regional station measurements were generally 3–6 °C lower than those recorded at the in-situ measurement points. In summer, although the overall diurnal trends were similar, temperatures at the measurement points increased more rapidly, reaching daytime peak values of approximately 43 °C in the afternoon. During the transitional season, the weather station exhibited a daily temperature range of approximately 5 °C, whereas the range at the measurement points was approximately 10 °C. In winter,

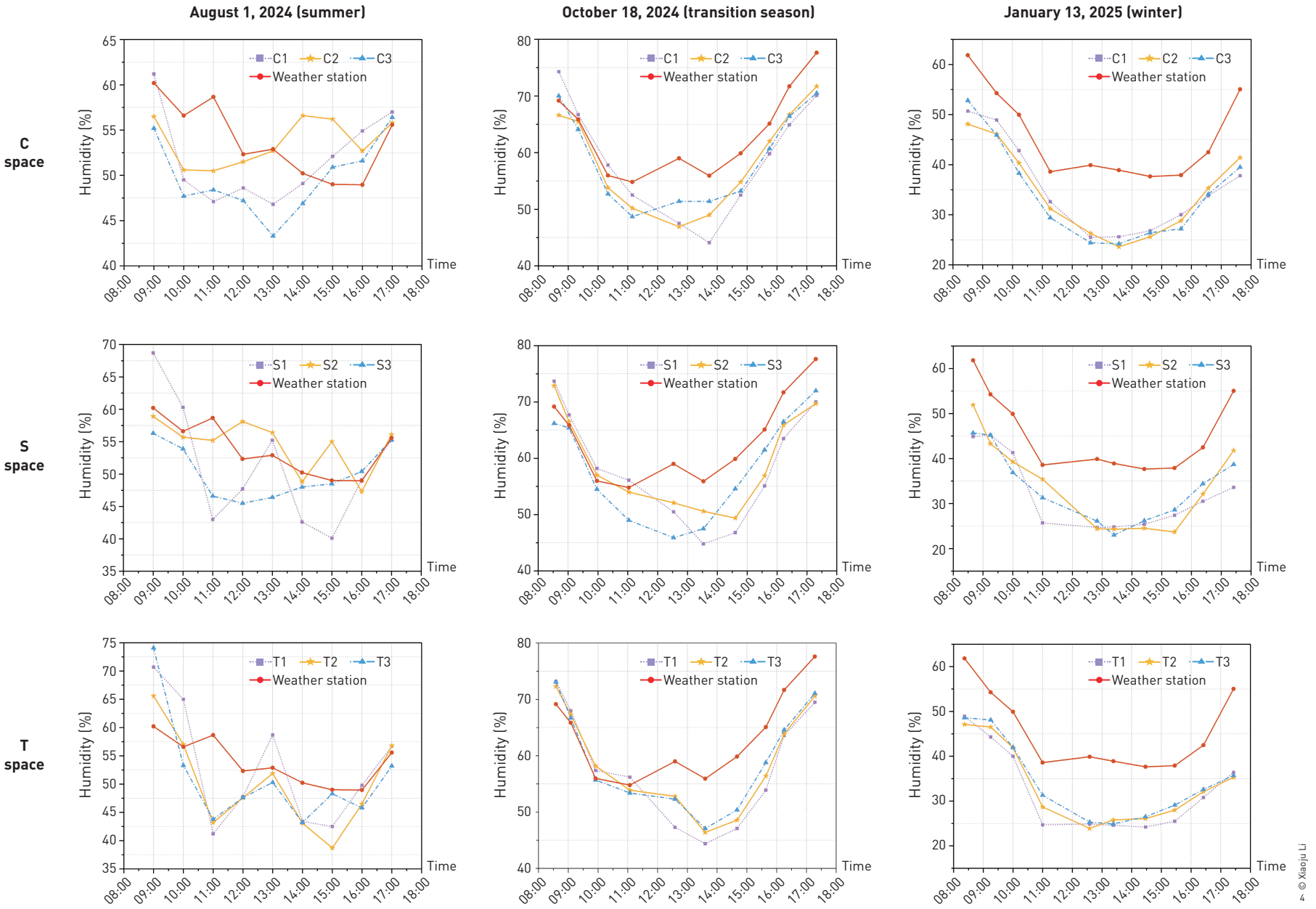


Fig. 4 Comparison of humidity between regional and local climate data.

temperatures at the neighborhood measurement points rose more rapidly than those recorded at the weather station, with daytime maximum temperatures reaching approximately 21 °C—about 6 °C higher than the station measurements during the same period.

Regarding relative humidity, a consistent pattern of "lower humidity within the neighborhood" was observed, with the regional weather station recording values approximately 8%–15% higher than those measured at the local sampling points. In summer, relative humidity at the weather station was approximately 60% at 8:00, gradually decreased as air temperature rose to a minimum of about 47% at 16:00, and then rebounded to approximately 55% at 18:00. Compared with the station data, humidity fluctuations at the measurement points were more pronounced. During the transitional season, the station recorded a humidity of approximately 68% at 8:00, which decreased to a minimum of about 56% at 11:00 and subsequently increased to approximately 75% at 18:00, with a daily variation of about 19%. In contrast, the mean humidity at the measurement points declined more rapidly, dropping to approximately 46% in the afternoon—around 10% lower than the station values during the same period. In winter, relative humidity at the measurement points remained consistently lower than that recorded at the weather station throughout the daytime.

In summary, the temperature and humidity distributions among the three spatial types exhibit clear differences. Across all

three seasons, the neighborhood demonstrates a characteristic pattern of "higher temperature and lower humidity" compared with regional background conditions, with this regulatory effect being most pronounced in summer. During peak midday heat, air temperature can increase by approximately 5 °C, while relative humidity decreases by 8%–15%, significantly affecting human thermal comfort. These findings indicate that the microclimatic characteristics of old urban blocks are highly dependent on spatial morphology, providing empirical support for subsequent simulation analyses and regeneration-oriented design strategies.

4.2 Microclimate Simulation and Validation

4.2.1 Analysis of Simulation Results

The simulation results indicate that the ground surface temperature in the study area exhibits a typical diurnal pattern. At 8:00, as solar altitude increases, the ground gradually absorbs solar radiation and temperature rise slowly, with an average increase of approximately 1–2 °C. Between 8:00 and 12:00, surface temperatures continue to increase rapidly, rising by about 5 °C overall and reaching a daily peak between 12:00 and 14:00 when solar radiation is most intense. Significant temperature differences are observed among surface types. Building rooftops and paved surfaces record the highest temperatures, approximately 2–4 °C higher than adjacent green spaces. In contrast, vegetated areas warm more gradually and maintain daytime temperatures 1–3 °C lower than paved area. From 14:00 to 18:00, as solar radiation intensity decreases, surface temperatures gradually decline by approximately 4 °C (Figs. 5, 6).

The simulation results not only validate the reliability of the field measurements but also more clearly reveal the differentiated thermal characteristics among the three representative spatial types. During the peak heat period at midday (12:00–14:00), a systematic temperature gradient is observed. Alley spaces exhibit strong orientation dependence. East–west alleys experience prolonged direct solar exposure and therefore show significantly higher surface temperatures. In contrast, narrow alleys or those oriented north–south benefit from continuous shading due to building obstruction, resulting in relatively lower and more stable temperatures. Courtyard spaces, which primarily consist of paved surfaces and higher sky view factors, heat up rapidly; however, courtyards containing vegetation maintain significantly lower temperatures than fully paved areas. Transitional spaces, owing to overhead shading elements that effectively block direct solar radiation, display smaller diurnal temperature fluctuations throughout the day.

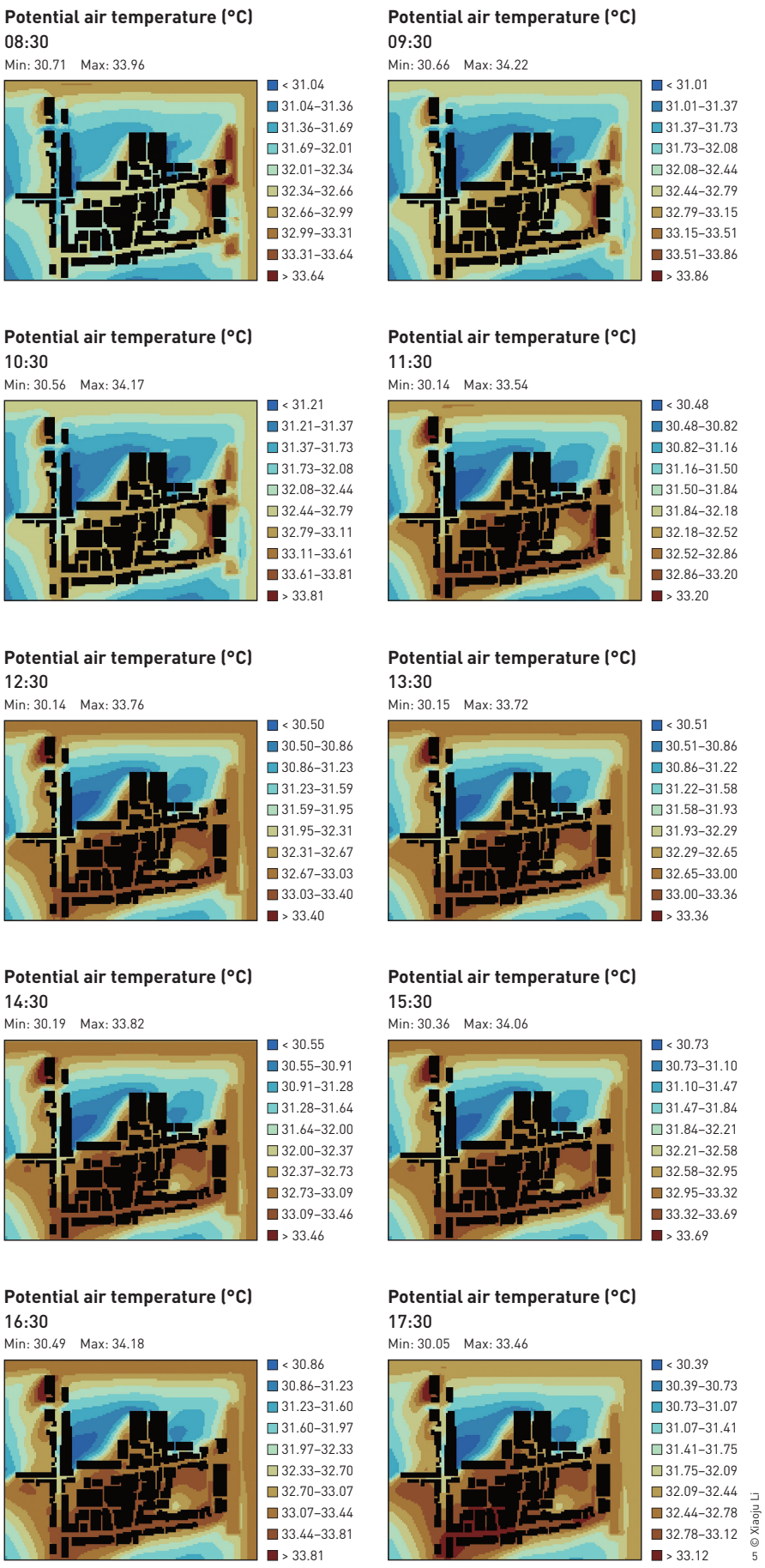


Fig. 5 ENVI-met summer simulation results.

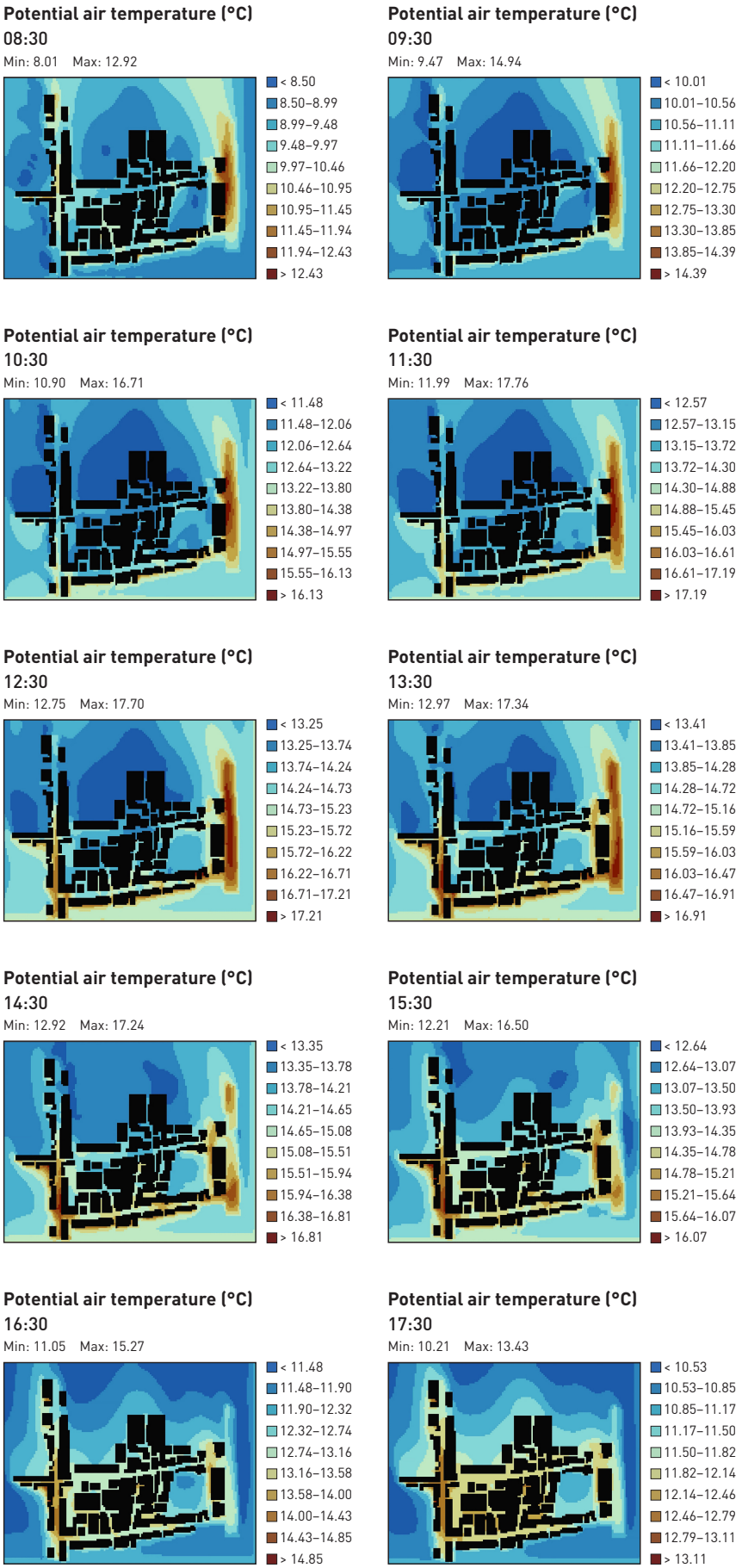


Fig. 6 ENVI-met winter simulation results.

© Xiaoju Li

4.2.2 Accuracy Verification and Error Evaluation

This section evaluates the reliability of the microclimate simulation results by conducting an accuracy assessment based on outputs from ENVI-met. A comparison between regional observational data, point-based field measurements, and ENVI-met simulation results shows strong agreement. The coefficients of determination (R^2) for the three seasons are 0.953, 0.948, and 0.955, respectively, all exceeding 0.94, which indicates a high level of consistency between simulated and observed data. The boxplots show that the fluctuation ranges of the three datasets are similar and partially overlapping, indicating that the simulated data are relatively well-concentrated and that the differences among the datasets are not statistically significant. This further confirms the reliability of the simulation results (Fig. 7).

Subsequently, an error evaluation analysis was conducted for the simulated air temperature and relative humidity at the measurement points within each spatial category. According to previous studies[38–39], when the RMSE of air temperature ranges from 0.52 °C to 4.30 °C and the prediction error of relative humidity does not exceed 6.4%, the discrepancy between simulated and measured values is considered relatively small. The results show that the RMSE values for air temperature across all spatial types in this study are below 2.0 °C, while the RMSE values for relative humidity are all below 5%. Additionally, the MAPE for both variables is less than 10% (Table 3). The RMSE and MAPE values at all measurement points fall within acceptable ranges, indicating that the ENVI-met simulation results accurately reflect the observed conditions. Therefore, the application of ENVI-met for outdoor microclimate simulation in this study is reliable.

4.3 Spearman Correlation Analysis

The Spearman correlation test results indicate that the majority of indicators (13 out of 20) show statistically significant correlations with UTCI ($p < 0.05$). However, their correlation coefficients are generally weak (mean $|\rho| < 0.25$) (Table 4). Although the direction of correlation varies slightly across different seasons, no stable and consistent monotonic trend is observed. Among all variables, a few indicators (i.e., RD, SVF, FAI, NL, PAR) exhibit relatively higher correlation coefficients; however, even these fail to demonstrate a clear monotonic association with the UTCI. Overall, these findings suggest that the relationship between urban morphology and human thermal comfort is not characterized by a simple monotonic response. To further uncover potential nonlinear interaction patterns, it is necessary to integrate subsequent model outputs and SHAP-based interpretative analysis.

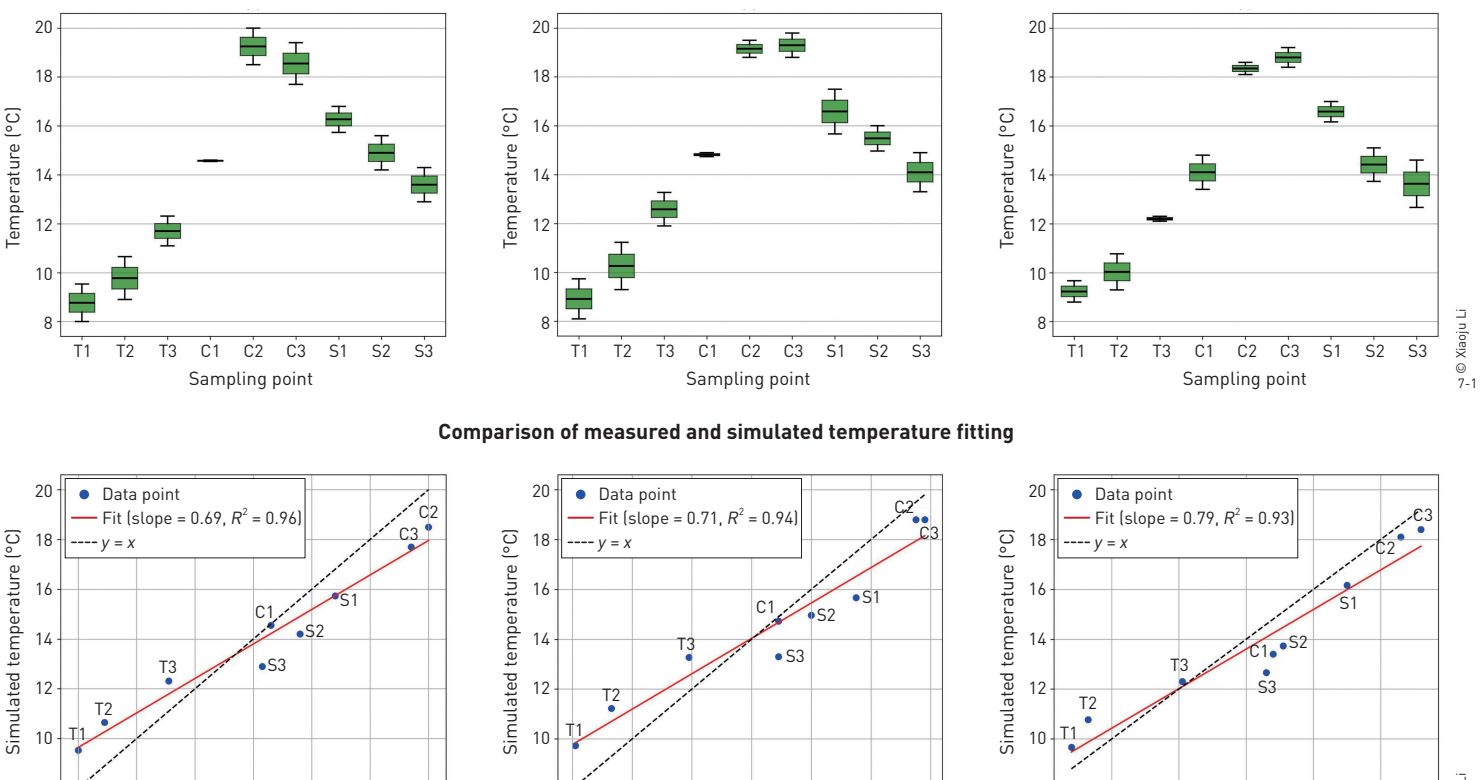


Fig. 7 Linear fitting of simulated and measured temperatures.

Table 3: Error evaluation results of simulated data

Space category	RMSE		MAPE	
	Temperature (°C)	Humidity (%)	Temperature (°C)	Humidity (%)
C	1.15	1.81	1.15	1.81
S	0.86	2.07	0.86	2.07
T	1.08	2.54	1.08	2.54

4.4 Nonlinear Correlation Analysis

Due to large summer measurement errors (e.g., thermal drift, airflow disturbances), only winter data were used for the nonlinear mechanism analysis. Building upon the Spearman correlation results, this study employed the XGBoost–SHAP approach to conduct a nonlinear regression analysis. Based on the fishnet grid framework, urban spatial morphology data were integrated with microclimate simulation outputs from ENVI-met to evaluate the global contributions of 20 urban morphological indicators to

Table 4: Spearman's coefficients of morphological indicators with UTCI

Indicator	Correlation coefficient (ρ)	Indicator	Correlation coefficient (ρ)
HW	–0.136*	BL	–0.116
DH	–0.150*	SVF	0.174*
RD	–0.174*	PAFRAC	0.134*
GR	0.154*	K	–0.053
NP	0.162*	VI	–0.098
PAR	0.170	LC	–0.131*
LA	0.154*	LI	–0.119
Street θ	–0.117	HMD	–0.123*
FAI	–0.158*	RE	–0.136*
A_SD	–0.079	NL	0.162*

NOTE

* indicates the correlation is significant at the 0.05 level (two-tailed).

courtyard thermal comfort (Fig. 8). Figure 8-1 presents the ranking of features according to their mean absolute SHAP values. Among all variables, SVF exhibits the highest mean SHAP value (0.13413), indicating the greatest contribution to model predictions, whereas HMD shows the lowest value (0.00421), suggesting minimal influence. Figure 8-2 further quantifies feature importance based on the mean absolute SHAP values, revealing that SVF, FAI, NL, and PAR contribute most significantly. Although VI ranks third among the indicators, as a visual connectivity metric with weak relevance to winter thermal comfort and limited semantic segmentation accuracy in winter, it was not included in the detailed discussion of this subsection. Notably, the top four features display alternating positive and negative contributions, suggesting that their effects on local human thermal comfort are characterized by nonlinear and threshold-dependent relationships.

4.5 Influence Mechanisms Based on SHAP Values

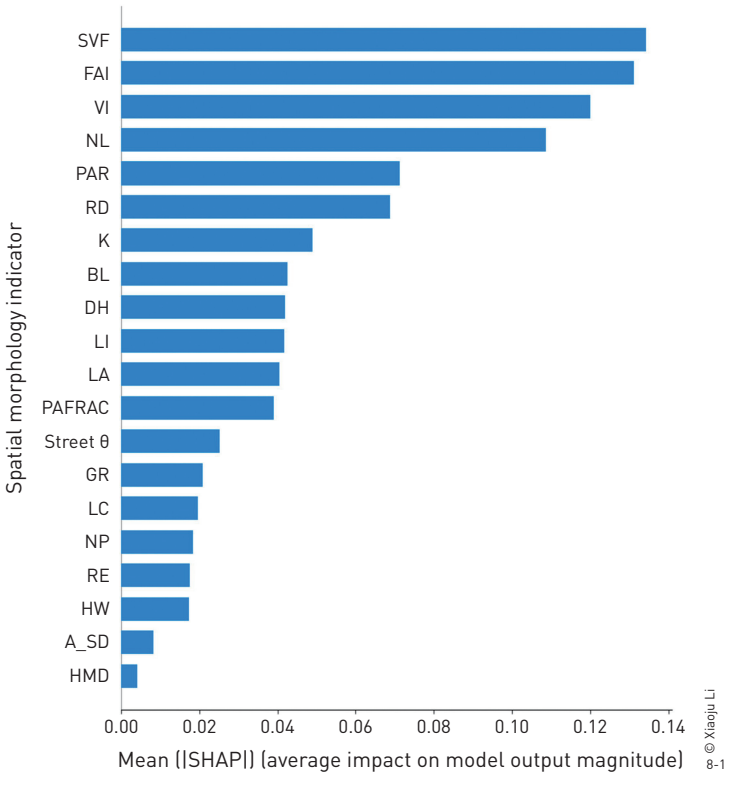
Based on the joint evaluation of Spearman correlation and XGBoost–SHAP global contributions, four key morphological factors—SVF, NL, PAR, and FAI—were ultimately identified as the core determinants of outdoor thermal comfort in winter. To clarify the specific mechanisms on the UTCI, the LOWESS method was employed to construct SHAP-based local dependence plots for 19 morphological indicators. Because low-angle winter sunlight introduces substantial uncertainty in the directional definition of Street θ, its physical interpretation is unclear. Hence, it was not included in the graphical analysis of this subsection. These plots illustrate the marginal effects of variations in feature values on the model output, as well as the direction and magnitude of each feature's contribution to UTCI across different value ranges.

Through detailed analysis of the four core factors' SHAP local dependence curves, the nonlinear response patterns and threshold characteristics of winter urban canyon morphology on outdoor thermal comfort are quantitatively revealed.

4.5.1 Sky View Factor (SVF)

Figure 9 indicates that SVF exhibits a nonlinear relationship with thermal comfort, with different response tendencies across value ranges. The following interpretation is primarily based on the density-aware LOWESS fitting curve.

Firstly, when SVF is below approximately 0.2, SHAP values gradually decrease, suggesting that highly enclosed street environments experience progressively poorer ventilation as enclosure increases. This finding is consistent with previous studies which noted that highly enclosed street canyons tend to suppress air movement and thereby worsen comfort conditions[40–41]. Secondly, when SVF increases from approximately 0.20 to 0.45, SHAP values show a slight upward increase, indicating



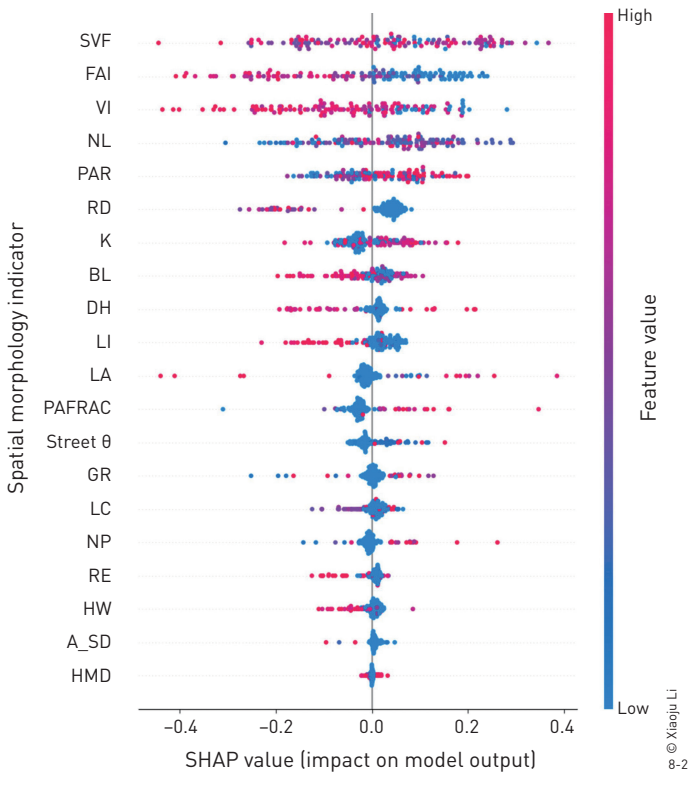


Fig. 8 Winter nonlinear regression analysis based on the XGBoost-SHAP model.

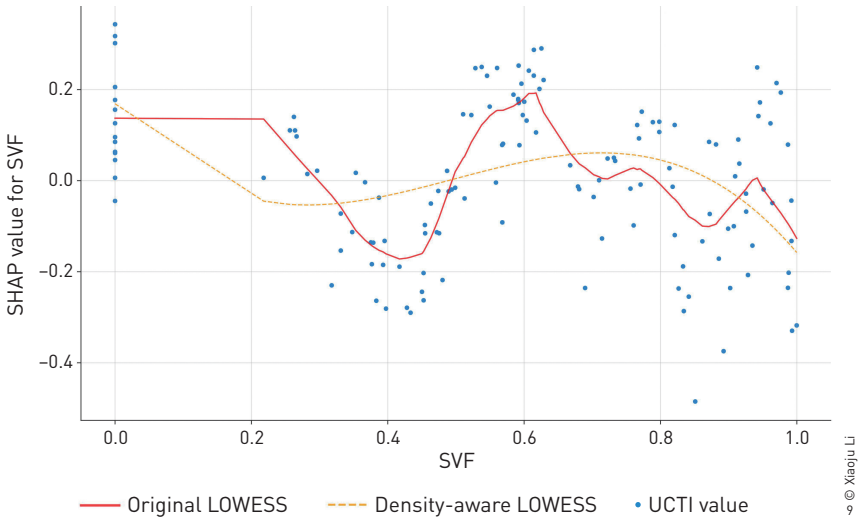


Fig. 9 Local dependence analysis of SVF indicator based on LOWESS.

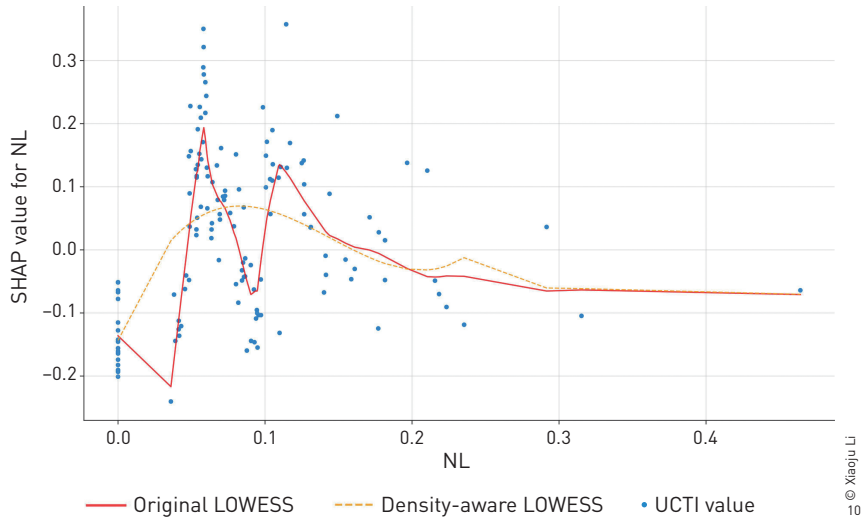


Fig. 10 Local dependence analysis of NL indicator based on LOWESS.

that incremental increases in openness within relatively compact environments may begin to improve airflow and mitigate heat accumulation. Thirdly, a clearer positive relationship emerges when SVF ranges approximately between 0.45 and 0.80, during which SHAP values gradually increase. In this interval, reduced building enclosure improves ventilation and convective heat exchange, while moderate solar access contributes to enhanced outdoor environmental quality. However, when SVF exceeds approximately 0.8, SHAP values decline again, indicating that excessive spatial openness may weaken shading performance and increase direct solar exposure under outdoor conditions, thereby reducing thermal comfort.

These results suggest that the relatively favorable SVF range for outdoor thermal comfort appears to be approximately 0.55–0.75, within which ventilation improvement and solar exposure remain comparatively balanced. By contrast, excessively enclosed or overly open spaces may both negatively influence outdoor comfort.

4.5.2 Near-Linearity Ratio (NL)

Figure 10 indicates that NL exhibits a pronounced nonlinear relationship with thermal comfort. The following interpretation is primarily based on the density-aware LOWESS fitting curve.

Firstly, when NL values are extremely low (below approximately 0.03), SHAP values remain relatively negative, suggesting that overly open street environments may expose pedestrians to excessive solar radiation under outdoor conditions, thereby reducing thermal comfort. Secondly, as NL increases to approximately 0.03–0.08, SHAP values rise noticeably and reach a local peak. This trend suggests that a moderate increase in spatial enclosure can improve shading performance while maintaining relatively adequate ventilation conditions. The combined effects of reduced solar exposure and acceptable airflow contribute positively to outdoor thermal comfort. Thirdly, when NL exceeds approximately 0.1, SHAP values gradually decline again. Increased building density and spatial enclosure may weaken airflow and restrict convective heat dissipation, while excessive shading can also reduce environmental openness and natural daylight availability. As a result, thermal comfort tends to deteriorate under highly enclosed street conditions. Finally, when NL further increases beyond approximately 0.2, the SHAP curve gradually stabilizes, indicating that the marginal influence of additional enclosure on thermal comfort becomes weaker. This suggests that the thermal response to NL may approach a relatively stable state under highly compact urban forms.

Overall, the results suggest that moderately enclosed street environments are more favorable for outdoor thermal comfort under the hot–humid climatic conditions of southern Zhejiang. The relatively suitable NL range appears to be approximately 0.03–0.10, within which shading benefits and ventilation performance remain comparatively balanced.

4.5.3 Frontal Area Index (FAI)

Figure 11 indicates that FAI exhibits a nonlinear relationship with thermal comfort, with different response tendencies across varying value ranges. The following interpretation is primarily based on the density-aware LOWESS fitting curve.

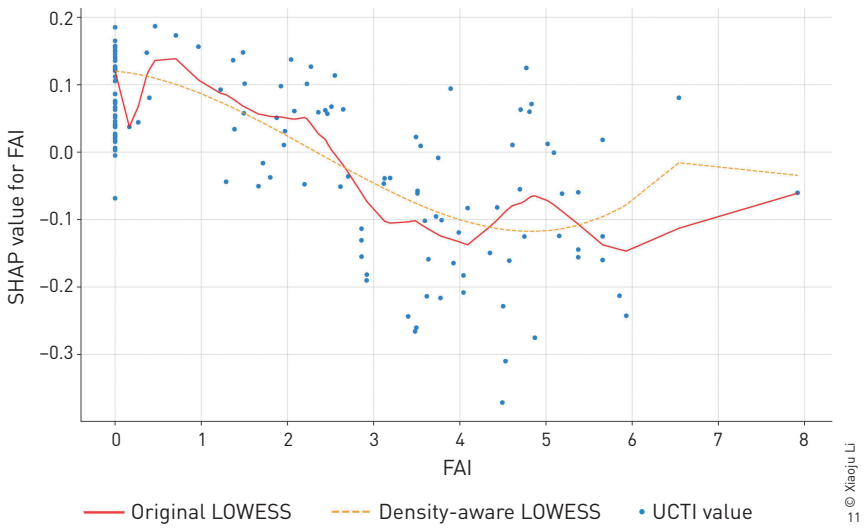


Fig. 11 Local dependence analysis of FAI indicator based on LOWESS.

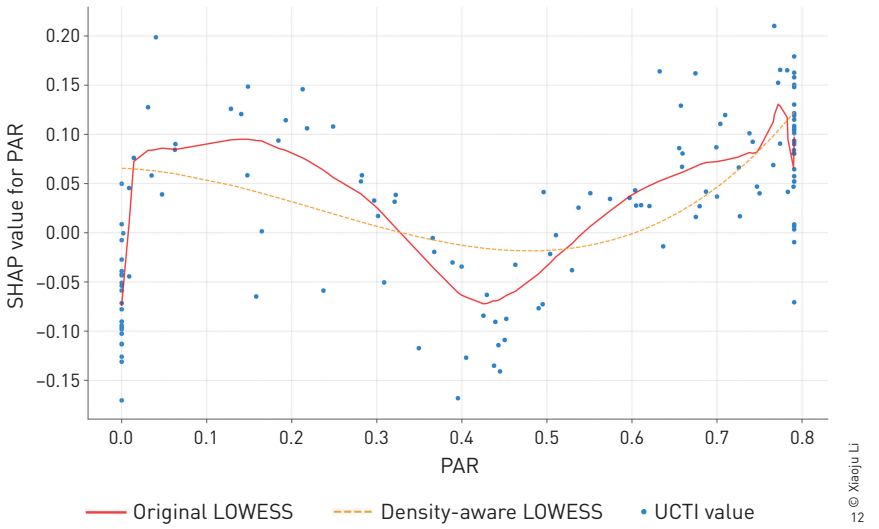


Fig. 12 Local dependence analysis of PAR indicator based on LOWESS.

Firstly, when FAI remains relatively low (approximately below 0.5–1.0), SHAP values are generally positive, suggesting that lower frontal area obstruction is associated with improved airflow conditions and enhanced outdoor thermal comfort. Under relatively open spatial configurations, air movement can facilitate convective heat dissipation and reduce local heat accumulation. Secondly, as FAI increases from approximately 1.0 to 4.0, SHAP values show an overall downward trend. Increased frontal area obstruction may weaken urban ventilation efficiency by reducing wind speed and restricting airflow pathways. Consequently, reduced convective cooling capacity contributes to deteriorated thermal comfort under hot–humid outdoor conditions. Thirdly, when FAI exceeds approximately 4.0, the SHAP curve exhibits slight fluctuations and a weak rebound tendency. However, the sample density within this interval is relatively limited, indicating that the relationship between extremely high FAI values and thermal comfort may involve greater local variability and uncertainty.

The results suggest that excessive frontal area obstruction generally exerts a negative influence on outdoor thermal comfort in southern Zhejiang. A relatively favorable FAI range appears to be approximately 0.3–1.0, within which ventilation performance and spatial openness remain comparatively balanced, thereby contributing to reduced outdoor thermal stress.

4.5.4 Paved Area Ratio (PAR)

Figure 12 indicates that PAR exhibits a pronounced nonlinear relationship with thermal comfort and demonstrates evident threshold characteristics. The following interpretation is primarily based on the density-aware LOWESS fitting curve.

Firstly, when PAR is in the range of approximately 0.2–0.5, SHAP values gradually decline, indicating that expanded paved coverage may intensify surface heat storage and sensible heat release under outdoor conditions. Increased impervious surfaces can weaken evaporative cooling capacity and contribute to higher thermal stress, thereby reducing outdoor thermal comfort. Secondly, when PAR further rises to approximately 0.5–0.8, SHAP values exhibit a renewed upward tendency. This trend suggests that the thermal effects of paved surfaces may also depend on differences in paving materials, surface reflectivity, permeability, and local spatial configurations. Optimized pavement strategies, such as permeable or reflective materials, may partially mitigate heat accumulation and improve outdoor environmental conditions.

Overall, a relatively favorable PAR range appears to be approximately 0.1–0.3, within which paved surfaces remain limited while excessive heat accumulation is effectively avoided.

5 Discussion and Conclusions

This study systematically examined the influence of spatial morphology on human thermal comfort based on seasonal microclimate observations and ENVI-met simulations in the old urban block of Cangqian Street, Rui'an, proposing actionable quantitative indicators for urban regeneration. The results indicate that SVF exhibits evident threshold-dependent characteristics under winter climatic conditions in southern Zhejiang. A relatively favorable SVF range appears to be approximately 0.55–0.75,

within which solar radiation access and environmental openness remain comparatively balanced. For NL, moderately enclosed street environments appear more conducive to winter thermal comfort, with a relatively suitable range of approximately 0.03–0.10, likely due to their combined effects on wind protection and spatial enclosure. Regarding FAI, excessive frontal area obstruction may weaken environmental openness and airflow efficiency, whereas relatively lower FAI conditions appear more favorable for maintaining balanced thermal conditions. A relatively favorable FAI range appears to be approximately 0.3–1.0. PAR also demonstrates evident nonlinear and threshold-dependent characteristics. Lower PAR conditions are generally associated with improved outdoor thermal comfort, while excessive paved surfaces may contribute to unfavorable surface thermal conditions. The relatively favorable PAR range appears to be approximately 0.1–0.3.

Comparisons with previous studies show that the quantitative findings of this research broadly align with several empirical and simulation-based investigations[42–44]. However, an empirical study[45] indicated that although lower SVF may reduce daytime air temperatures, it can also weaken nocturnal cooling capacity. This highlights an inherent diurnal trade-off in SVF regulation. Therefore, practical applications must account for local climatic characteristics to balance the dual objectives of daytime shading and nighttime cooling. Additionally, some canyon-scale numerical simulation studies suggest that increasing windward openness and ventilation efficiency effectively alleviates summer thermal discomfort[46]. Consistent with these findings, the present study shows that excessively high FAI values may intensify thermal stress, implying that the regulatory effects of the wind environment are jointly constrained by background climate conditions, humidity levels, and the enclosure characteristics of street canyons.

Based on these findings, this study proposes practical microclimate optimization strategies. At the urban planning and design levels, the recommended indicator ranges can be incorporated into local design guidelines and regeneration regulations to inform block layout, street orientation, building density control, and ventilation corridor planning. This enables coordinated improvements in the thermal environment, wind environment, and stormwater management. During the implementation of old urban block regeneration, these strategies are particularly applicable to old urban blocks in coastal county towns of southeast Zhejiang, which often adopt incremental and low-cost regeneration approaches. Through localized adjustments—such as optimizing building spacing, refining street height-to-width ratios, replacing impervious pavements, and increasing green coverage—it is possible to substantially enhance climate resilience and alleviate summer heat and winter cold stress while preserving the original urban fabric and social structure.

The core innovations of this study are reflected in three aspects. First, an integrated assessment framework was established by coupling long-term field measurements, multi-season ENVI-met simulations, and quantified spatial morphological indicators, enabling a refined correspondence between block-scale microclimate processes and spatial form characteristics. Second, the seasonal response characteristics of key morphological factors (SVF, NL, FAI, and PAR) were quantitatively identified, and threshold ranges with practical implications for human thermal comfort were proposed. Third, complex microclimate regulation mechanisms were translated into actionable urban regeneration design parameters and spatial optimization strategies. This provides a quantifiable and implementable technical pathway for climate-adaptive design in old urban blocks undergoing stock-based urban regeneration.

Although limitations remain regarding sample diversity, nighttime climate representation, and the coupling of material parameters, the established indicator system and strategic framework provide a foundation for subsequent research and design practice across different climate zones and for old urban blocks in coastal county towns of southeast Zhejiang. Future studies could enhance precision and generalizability by expanding observation coverage, extending monitoring periods, and incorporating multi-factor coupled simulations.

ELECTRONIC SUPPLEMENTARY MATERIAL

Supplementary material is available in the online version of this article at https://doi.org/10.15302/J-LAF-2026-0025.

Competing interests | The authors declare that they have no competing interests.

REFERENCES

[1] McGranahan, G., & Satterthwaite, D. (2014). *Urbanisation concepts and trends*. IIED.

[2] State Council of the People's Republic of China. (2021, March 12). *Government work report*.

[3] National Development and Reform Commission of the People's Republic of China. (2022, July 28). *New urbanization implementation scheme during the 14th Five-Year Plan*.

[4] State Council of the People's Republic of China. (2024, July 28). *Notice on the five-year action plan for deepening the implementation of the people-oriented new urbanization strategy*.

[5] General Office of the Ministry of Finance & General Office of the Ministry of Housing and Urban-Rural Development of the People's Republic of China. (2025, April 3). *Notice on the implementation of urban renewal supported by the central government in 2025*.

[6] Onyango, A. O. (2018). Global and regional trends of urbanization: A critical review of the environmental and economic imprints. *World Environment*, *8*(2), 47–62.

[7] Zheng, H. W., Shen, G. Q., & Wang, H. (2014). A review of recent studies on sustainable urban renewal. *Habitat International*, *41*(1), 272–279.

[8] Wang, W., Wang, S., Chen, H., He, J., & Mao, L. (2025). Exploring the characteristics of influencing factors and mitigation strategies for surface urban heat island intensity in four cities in China based on machine learning and local climate zones. *Environmental Science*, *46*(12), 8093–8104.

[9] De La Cruz, J., Solano Reynoso, W., Moncada, W., Soca Flores, R., Carrasco Badajoz, C., Rayme Chalco, C., & Lozano, J. (2025). Surface heat island and its link to urban morphology: Multitemporal analysis with Landsat images in an Andean City in Peru. *Urban Science*, *9*(12), 507.

[10] Jiang, C., Leng, H., & Yuan, Q. (2022). Construction of climate adaptability evaluation indicator system for urban spaces in the severe cold zones of China—A case study on the central area of Harbin. *Landscape Architecture Frontiers*, *10*(4), 45–69.

[11] Xiao, Y., Dai, S., & Zhao, B. (2020). Mitigation of urban heat island effect with small-scale parks—An empirical study on community parks in Nanjing, Jiangsu Province. *Landscape Architecture Frontiers*, *8*(3), 26–43.

[12] Zheng, J., Ou, Z., Xiang, Y., Li, J., & Zheng, B. (2025). How can street interface morphology effect pedestrian thermal comfort: A case study of the old town of Changsha, China. *Urban Climate*, *60*, 102341.

[13] Lopez-Cabeza, V. P., Loor-Vera, M. J., Diz-Mellado, E., Rivera-Gomez, C., & Galan-Marin, C. (2024). Decoding outdoor thermal comfort: The role of location in urban canyon microclimate. *Sustainable Energy Technologies and Assessments*, *72*, 104095.

[14] Okumus, D. E., & Akay, M. (2025). Quantitative assessment of non-stationary relationship between multi-scale urban morphology and urban heat. *Building and Environment*, *272*, 112669.

[15] Liu, H., Huang, B., Gao, S., Wang, J., Yang, C., & Li, R. (2021). Impacts of the evolving urban development on intra-urban surface thermal environment: Evidence from 323 Chinese cities. *Science of the Total Environment*, *771*, *144810*.

[16] Jiang, L., Liu, S., & Liu, C. (2021). The contributions of blue-green infrastructure to building urban climatic resilience—Bibliometric analysis based on co-citation networks. *Landscape Architecture Frontiers*, *9*(6), 8–23.

[17] Su, Y. M., & Antoni, J. (2023). Outdoor thermal comfort study on urban areas with various densities in Taipei. *Engineering Proceedings*, *38*(1), 77.

[18] Kamal, A., Abidi, S. M. H., Mahfouz, A., Kadam, S., Rahman, A., Hassan, I. G., & Wang, L. L. (2021). Impact of urban morphology on urban microclimate and building energy loads. *Energy and Buildings*, *253*, 111499.

[19] Pompei, L., Nardecchia, F., Gugliermetti, L., & Cinquepalmi, F. (2024). Design of three outdoor combined thermal comfort prediction models based on urban and environmental parameters. *Energy and Buildings*, *306*, 113946.

[20] Liu, Z., Jin, Y., & Jin, H. (2019). The effects of different space forms in residential areas on outdoor thermal comfort in severe cold regions of China. *International Journal of Environmental Research and Public Health*, *16*(20), 3960.

[21] Tsirigoti, D. (2025). Urban geometry and sustainability: The effect of green interventions on the urban microclimate of Greek cities. *Euro-Mediterranean Journal for Environmental Integration*, *10*, 4355–4367.

[22] Liu, Z., Li, J., & Xi, T. (2023). A review of thermal comfort evaluation and improvement in urban outdoor spaces. *Buildings*, *13*(12), 3050.

[23] Lindberg, F., Wallenberg, N., Thorsson, S., Haeger-Eugensson, M., Lönn, J., Holmberg, B., ... Fahlström, J. (2025). Micro-scale, city-wide analysis of outdoor thermal comfort during heatwaves in high latitude cities: Influence of building geometry and vegetation. *International Journal of Biometeorology*, *69*(12), 3421–3434.

[24] Zaki, S. A., Othman, N. E., Syahidah, S. W., Yakub, F., Muhammad-Sukki, F., Ardila-Rey, J. A., ... Mohd Saudi, A. S. (2020). Effects of urban morphology on microclimate parameters in an urban university campus. *Sustainability*, *12*(7), 2962.

[25] Zhou, S., Jia, W., Liu, Z., & Wang, M. (2024). Prediction and machine learning analysis of urban waterlogging risks in high-density areas from the perspective of the built environment: A case study of Shenzhen, China. *Landscape Architecture Frontiers*, *12*(5), 48–60.

[26] Pan, Y., Morimoto, T., & Ichinose, T. (2024). Combining multi-source satellite data with a microclimate model to analyze the microclimate of an urban park. *Climate*, *12*(12), 197.

[27] Zhao, X., & Lin, G. (2024). Research on the perception evaluation of urban green spaces using panoramic images and deep learning: A case study of Zhujiang park in Guangzhou. *Landscape Architecture Frontiers*, *12*(6), 7–18.

[28] Zhou, Y., & Zhang, Y. (2022). Research on the open-block-oriented control indexes of street interface morphology. *Time Architecture*, (1), 38–42.

[29] Li, X., & Zhang, Y. (2021). Combining the historico-geographical and configurational approaches to urban morphology: The historical transformations of Ludlow, UK and Chinatown, Singapore. *Urban*

Morphology, *25*(1), 23–41.

[30] Koutsanitis, S., Sinou, M., Kanetaki, Z., Tousi, E., & Varelidis, G. (2025). Thermal performance investigation in historical urban neighborhoods using ENVI-met simulation software. *Land*, *14*(2), 284.

[31] Fiala, D., Havenith, G., Bröde, P., Kampmann, B., & Jendritzky, G. (2012). UTCI-Fiala multi-node model of human heat transfer and temperature regulation. *International Journal of Biometeorology*, *56*(3), 429–441.

[32] Huang, Z., Liu, J., Luo, T., & Hong, X. (2021). Research on the spatial-temporal changes of regional morphology of residential neighborhoods in county-level cities of China: Cases studies on Qingcheng County, Wu'an City, Changxing County, Lianjiang County, and Jintang County. *Landscape Architecture Frontiers*, *9*(2), 12–25.

[33] Zheng, J., Du, Y., Zhu, X., & Dong, W. (2025). Mapping global human thermal comfort: Spatiotemporal variability of UTCI regions under climate change. *Sustainable Cities and Society*, *110*, 106111.

[34] Blazejczyk, K., Broede, P., Fiala, D., Havenith, G., Holmér, I., Jendritzky, G., ... Kunert, A. (2010). Principles of the new Universal Thermal Climate Index (UTCI) and its application to bioclimatic research in European scale. Miscellanea Geographica. *Regional Studies on Development*, *14*(1), 91–102.

[35] Uyar, S. G. K., Ozbay, B. K., & Dal, B. (2025). Interpretable building energy performance prediction using XGBoost quantile regression. *Energy and Buildings*, *340*, 115815.

[36] Lan, H., Hou, H. C., & Gou, Z. (2023). A machine learning led investigation to understand individual difference and the human-environment interactive effect on classroom thermal comfort. *Building and Environment*, *236*, 110259.

[37] Li, J., Lin, S., Kong, N., Ke, Y., Zeng, J., & Chen, J. (2024). Nonlinear and synergistic effects of built environment indicators on street vitality: A case study of humid and hot urban cities. *Sustainability*, *16*(5), 1731.

[38] Sinsel, T., Simon, H., Ouyang, W., dos Santos Gusson, C., Shinzato, P., & Bruse, M. (2022). Implementation and evaluation of mean radiant temperature schemes in the microclimate model ENVI-met. *Urban Climate*, *45*, 101279.

[39] Tsoka, S., Tsikaloudaki, A., & Theodosiou, T. (2018). Analyzing the ENVI-met microclimate model's performance and assessing cool materials and urban vegetation applications: A review. *Sustainable Cities and Society*, *43*, 55–76.

[40] He, H., Wang, H., Zheng, L., Zhao, T., Zhang, P., & Zheng, K. (2025). Factors and pathways to enhance resident satisfaction in old residential neighbourhood renovation: A configuration analysis of cases in central Nanchang, China. *Buildings*, *15*(7), 1125.

[41] Lin, T. P. (2009). Thermal perception, adaptation and attendance in a public square in hot and humid regions. *Building and Environment*, *44*(10), 2017–2026.

[42] Wu, J., Chang, H., & Yoon, S. (2022). Numerical study on microclimate and outdoor thermal comfort of street canyon typology in extremely hot weather—A case study of Busan, South Korea. *Atmosphere*, *13*(2), 307.

[43] Muniz-Gäal, L. P., Pezzuto, C. C., de Carvalho, M. F. H., & Mota, L. T. M. (2020). Urban geometry and the microclimate of street canyons in tropical climate. *Building and Environment*, *169*, 106547.

[44] Sun, C., Lian, W., Liu, L., Dong, Q., & Han, Y. (2022). The impact of street geometry on outdoor thermal comfort within three different urban forms in severe cold region of China. *Building and Environment*, *222*, 109342.

[45] Chen, L., Ng, E., An, X., Ren, C., Lee, M., Wang, U., & He, Z. (2012). Sky view factor analysis of street canyons and its implications for daytime intra-urban air temperature differentials in high-rise, high-density urban areas of Hong Kong: A GIS-based simulation approach. *International Journal of Climatology*, *32*(1), 121–136.

[46] Zhong, D., Gao, Y., Wei, L., Gu, X., Li, T., Xu, J., ... Liu, Z. (2025). Street canyon microclimate effect on thermal comfort at entrances and exits of underground commercial streets: Measured and ENVI-met simulation. *Buildings*, *15*(22), 4147.

LAF | https://doi.org/10.15302/J-LAF-2026-0025
第14卷 / 第3期 / 260025 / 2026
收稿日期 | 2025-10-15　录用日期 | 2026-03-06
中图分类号 | TU984　文献标识码 | A

基于多季节实证分析的浙东南沿海县城老旧街区热环境响应机制研究

李智兴[1,2,*]，李晓菊[1]，田密蜜[1]

1 浙江工业大学设计与建筑学院，杭州 310000
2 意大利米兰理工大学建筑环境与建造学院，米兰 20133

***通信作者**
地址：杭州市西湖区留和路288号浙江工业大学屏峰校区
邮编：310000
邮箱：zxlee910@zjut.edu.cn

摘要

本研究以浙江省瑞安市典型老旧街区为对象，探讨城市外部形态与人体热舒适度的量化关系，旨在建立适用于沿海县城老旧街区的城市更新评价指标体系。研究通过为期全年的实测调研与微气候模拟，构建夏季、过渡季与冬季的长时序动态监测序列，并提取20个空间形态量化指标，结合UTCI指标建立XGBoost-SHAP非线性回归模型。结果表明：1）三季下空气温度、湿度与风速因空间形态差异而发生显著变化；2）天空可视因子（SVF）、迎风面积指数（FAI）、硬质铺装比（PAR）与近线率（NL）为影响庭院热舒适度的关键因素；3）不同空间形态量化指标在不同的季节下对热舒适度的作用存在显著差异——对冬季而言，SVF宜为0.55~0.75，NL宜为0.03~1.0，FAI宜为0.3~1.0，PAR宜为0.1~0.3，以在遮阳、通风、保温与地表热环境之间取得平衡。研究在理论上丰富了微气候与空间形态关系的定量研究，在实践上提出了针对性优化策略，为浙东南沿海县城老旧街区的低碳更新与社区可持续发展提供了数据支撑与参考。

关键词

热舒适性；城市空间形态；微气候模拟；XGBoost-SHAP模型

文章亮点

- 构建融合实测、模拟与形态量化的综合微气候评估框架
- 量化SVF、NL、FAI与PAR的季节热响应及热舒适阈值
- 将微气候机制转化为面向更新实践的城市设计策略

基金项目

国家自然科学基金（编号：52308039）